Three-dimensional relativistic electron scattering in an ultrahigh-intensity laser focus

F. V. Hartemann,[1,2] J. R. Van Meter,[1,2,3] A. L. Troha,[1,2] E. C. Landahl,[1,2] N. C. Luhmann, Jr.,[2]
H. A. Baldis,[1,2] Atul Gupta,[4] and A. K. Kerman[5]
[1]*Institute for Laser Science and Applications, Lawrence Livermore National Laboratory, Livermore, California 94550*
[2]*Department of Applied Science, University of California, Davis, California 95616*
[3]*Department of Physics, University of California, Davis, California 95616*
[4]*Department of Electrical Engineering, The City College of New York, New York, New York 10031*
[5]*Department of Physics and Center for Theoretical Physics, Massachusetts Institute of Technology, Cambridge, Massachusetts 02139*

(Received 9 February 1998; revised manuscript received 28 May 1998)

The relativistic dynamics of an electron submitted to the three-dimensional field of a focused, ultrahigh-intensity laser pulse are studied numerically. The diffracting field in vacuum is modeled by the paraxial propagator and exactly satisfies the Lorentz gauge condition everywhere. In rectangular coordinates, the electromagnetic field is Fourier transformed into transverse and longitudinal wave packets, and diffraction is described through the different phase shifts accumulated by the various Fourier components, as constrained by the dispersion relation. In cylindrical geometry, the radial dependence of the focusing wave is described as a continuous spectrum of Bessel functions and can be obtained by using Hankel's integral theorem. To define the boundary conditions for this problem, the beam profile is matched to a Gaussian-Hermite distribution at focus, where the wave front is planar. Plane-wave dynamics are verified for large f numbers, including canonical momentum invariance, while high-energy scattering is predicted for smaller values of f at relativistic laser intensities. [S1063-651X(98)08210-5]

PACS number(s): 41.75.Ht, 42.25.Bs, 52.40.Nk, 42.55.−f

I. INTRODUCTION

The physics of laser-electron interactions [1–18] changes dramatically at relativistic intensities, where the transverse momentum of the charge, measured in electron units, exceeds one. Three fundamental processes are known to occur in this regime: nonlinear ponderomotive [16–18] and Compton [19,20] scattering, and high-intensity Kapitza-Dirac scattering [21,22]. These vacuum interactions correspond to the following geometries: collinear propagation, head-on collision, and electron diffraction in a laser standing wave, respectively.

An accurate description of the three-dimensional focus of a laser wave, in both the near-field and far-field regions, is required to properly describe the interaction of the electromagnetic field with charged leptons. In particular, the validity of the paraxial ray approximation [23–25], when used to model problems involving relativistic electrons copropagating with a laser wave over many Rayleigh ranges, must be firmly established. For applications involving ultrahigh-intensity [19] and nonlinear [20] Compton scattering, such as the γ-γ collider or focused x-ray sources, a detailed knowledge of the three-dimensional electromagnetic field distribution in the focal region is of paramount importance since the axial component of the fields may play a major role in the electron dynamics. An accurate field distribution is also required to properly model experimental results. Two ultrahigh-intensity relativistic electron scattering experiments are currently under way at the Stanford Linear Accelerator Center (SLAC) and the Commissariat à l'Energie Atomique (CEA). In the first case, nonlinear (multiphoton) Compton backscattering is investigated using the SLAC 50-GeV beam and a tightly focused terawatt-class laser [26]; at the CEA, low-energy electrons are accelerated by a terawatt laser [27]. In both instances, the three-dimensional nature of the focused laser pulse is an essential feature of the experiment and must be described accurately to interpret the resulting data correctly. In addition, considerable interest has been given recently to the detailed properties of laser focusing, partly because of potential applications such as plasma [28–33] and vacuum-based laser acceleration schemes [1–18]. For example, super-Gaussian rings have been thoroughly studied in an analysis [34] that shares some similarities with the present work. More in line with our motivation, the effect of the ponderomotive potential [35–37] associated with an ultrahigh-intensity laser wave on the radial confinement of relativistic electrons copropagating with the pulse has been investigated by Moore [38]. This analysis indicates that higher-order Gaussian modes can indeed confine the electrons through the focus because of the inward radiation pressure gradient. In this particular case, an accurate three-dimensional field distribution, satisfying both the vacuum wave equation and the gauge condition, is needed to conclusively demonstrate the validity of this approach.

An important goal of this paper is to present a comprehensive theoretical and numerical description of the relativistic dynamics of a charged particle interacting with an external electromagnetic field propagating *in vacuo*. To accurately describe the focusing and diffraction of the drive laser wave in vacuum, the paraxial propagator approach is used, where the mass shell condition (vacuum dispersion relation) is approximated by a quadratic Taylor expansion in the 4-wave-number [23–25]. This approach proves extremely accurate for any realizable laser focus and yields analytical expressions for the fields. In addition, the gauge condition is exactly satisfied everywhere, thus yielding a

proper treatment of the axial electromagnetic field components due to wave-front curvature. The electron phase is used as the independent variable, thus allowing for particle tracking over an arbitrarily large number of Rayleigh ranges, independent of the nonlinear slippage and relativistic Doppler shift due to radiation pressure. Ultrahigh-intensity ponderomotive scattering is studied as an example to demonstrate the relevance of this theoretical approach and the efficiency of the numerical algorithm developed here. The three-dimensional dynamics are different from earlier two-dimensional models [16,18,27]; in particular, the angular distribution of scattering energy no longer reflects canonical momentum invariance, as the light-cone variable is not invariant for focusing waves.

This paper is organized as follows. A brief review of the dynamics of an electron subjected to an ultrahigh-intensity plane wave in vacuum is given in Sec. II and the Lawson-Woodward theorem [15] is discussed, as is the scattering angular correlation described in references [16, 18, 27]. The general formalism used to obtain an exact three-dimensional solution to the wave equation in vacuum is described in Sec. III, with a special emphasis on rectangular coordinates, and the paraxial ray approximation is shown to derive from a simple Taylor expansion in the transverse wave number. In addition, the axial field component required to satisfy the gauge condition is analytically derived; this solution exactly satisfies the gauge condition everywhere. For completeness, the cylindrical wave equation in vacuum [39] is reviewed in the Appendix, and the corresponding vacuum eigenmode expansion is also presented there, as are the corresponding dispersion relations, together with the Fourier-Bessel transform of the focal field distribution, which is performed by using Hankel's integral theorem [40]. In Sec. IV, the relativistic electron dynamics in the three-dimensional paraxial fields are studied theoretically and numerically, and relativistic ponderomotive scattering is discussed within this framework. Finally, conclusions are drawn in Sec. V.

II. PLANE-WAVE DYNAMICS AND THE LAWSON-WOODWARD THEOREM

This section is intended as a brief review of the interaction of a relativistic electron with an ultrahigh-intensity plane wave. Further details can be found in Refs. [1–18].

The electron 4-velocity and 4-momentum are defined as [41,42]

$$u_\mu=\frac{1}{c}\frac{dx_\mu}{d\tau}\equiv\gamma(1,\boldsymbol{\beta}),\quad p_\mu=m_0cu_\mu,\quad u_\mu u^\mu=-1, \tag{1}$$

where τ is the proper time along the electron world line $x_\mu(\tau)$. In the absence of radiative corrections, the energy-momentum transfer equations are driven by the Lorentz force

$$\frac{du_\mu}{d\tau}=-\frac{e}{m_0c}(\partial_\mu A_\nu-\partial_\nu A_\mu)u^\nu. \tag{2}$$

For plane waves, the 4-vector potential of the laser wave is given by

$$A_\mu(\phi)=[0,\mathbf{A}_\perp(\phi)],\quad \phi=k_\mu x^\mu(\tau), \tag{3}$$

where ϕ is the relativistically invariant phase of the traveling wave along the electron trajectory. Note that the temporal dependence of the wave is arbitrary. Choosing $k_\mu\equiv(\omega_0/c)(1,0,0,1)$, with the wave propagating in the z direction, we have

$$\frac{d\phi}{d\tau}=\omega_0(\gamma-u_z)=\omega_0\kappa, \tag{4}$$

which defines the light-cone variable κ, and the 4-momentum transfer equations read

$$\frac{d\mathbf{u}_\perp}{d\tau}=\omega_0\kappa\frac{d}{d\phi}\left[\frac{e\mathbf{A}_\perp(\phi)}{m_0c}\right], \tag{5}$$

$$\frac{du_z}{d\tau}=\frac{d\gamma}{d\tau}=\omega_0\mathbf{u}_\perp\cdot\frac{d}{d\phi}\left[\frac{e\mathbf{A}_\perp(\phi)}{m_0c}\right]. \tag{6}$$

In the above, ω_0 is the characteristic laser frequency. Equation (6) shows that κ is invariant: $\kappa=\kappa_0=\gamma_0(1-\beta_0)$; additionally, Eq. (5) is readily integrated to yield the transverse momentum invariant

$$\mathbf{u}_\perp(\tau)=\frac{e\mathbf{A}_\perp(\phi)}{m_0c} \tag{7}$$

and the energy and axial momentum are immediately obtained using the fact that the 4-velocity is a unit 4-vector ($\gamma^2=1+\mathbf{u}_\perp^2+u_z^2$)

$$u_z(\tau)=\gamma_0\left\{\beta_0+\left[\frac{e\mathbf{A}_\perp(\phi)}{m_0c}\right]^2\left(\frac{1+\beta_0}{2}\right)\right\}, \tag{8}$$

$$\gamma(\tau)=\gamma_0\left\{1+\left[\frac{e\mathbf{A}_\perp(\phi)}{m_0c}\right]^2\left(\frac{1+\beta_0}{2}\right)\right\}. \tag{9}$$

These results are quite general and hold as long as plane waves are considered. An important difference between polarization states immediately appears: The square of the vector potential varies adiabatically as the pulse envelope for circular polarization, while there is an extra modulation at $2\omega_0$ for linear polarization. The transverse electron momentum depends linearly on the laser field, but the axial momentum is a quadratic function of that field, as it results from the coupling of the transverse velocity to the laser magnetic field through the ponderomotive force. This quadratic dependence of the energy and axial momentum on the 4-vector potential, measured in electron units, distinguishes the relativistic scattering regime, where $|e\mathbf{A}_\perp/m_0c|\geqslant 1$. In this regime, the ponderomotive force dominates the electron dynamics, yielding nonlinear slippage and Doppler shifts [19,20]. Equation (9) also provides a scaling for the maximum energy in a plane wave, $\gamma^*/\gamma_0\cong(e\mathbf{A}_\perp/m_0c)^2$, for relativistic electrons. Finally, the electron position is given by $\mathbf{x}(\phi)=(c/\omega_0)(1/\kappa_0)\int_0^\phi\mathbf{u}(\psi)d\psi$.

Equation (9) also shows that there is no net energy gained by the electron after interacting with a plane wave: We have $\lim_{\phi\to\infty}[\mathbf{A}_\perp(\phi)]=0$ and therefore $\lim_{\phi\to\infty}[\gamma(\phi)]=\gamma_0$. This is essentially the generalized version of the Lawson-Woodward theorem [15]. The fact that a charged particle cannot exchange energy and momentum with an incident

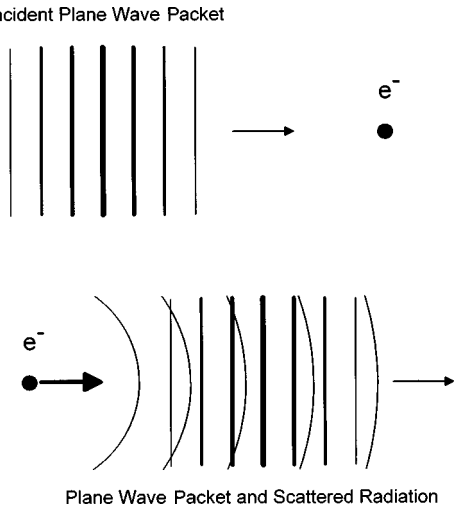

FIG. 1. Initial and final states for the interaction of a plane wave with an electron initially at rest.

plane wave in vacuum can also be easily understood. Consider a frame where the electron is initially at rest, as illustrated in Fig. 1. If the electron gains energy and momentum during the interaction, it is accelerated and therefore radiates. In the final state, the laser wave has been attenuated, which implies that there exists a permanent destructive interference between the laser wave and the wave radiated by the electron. This is the classical equivalent of photon annihilation in QED. However, the electron radiates waves that decay like r^{-2} and therefore no stable interference pattern can be obtained with a plane wave; in fact, in this case, any interference also decays like r^{-2}. This shows that, in the absence of radiative corrections (electron recoil), no net energy-momentum can be transferred from a plane wave to an electron in vacuum, in agreement with the generalized Lawson-Woodward theorem.

Finally, it also interesting to note that for plane waves, the electric and magnetic fields obey the relation $\mathbf{B}=(\mathbf{k}/\omega_0)\times\mathbf{E}=\hat{z}\times(\mathbf{E}/c)$, which results in the invariance of the light-cone variable. This in turn implies that there is a strict correlation between the electron trajectory angle $\theta=\arctan|\mathbf{u}_\perp/u_z|$ and its energy γ. Indeed, we have

$$u_\mu u^\mu=-1 \;\Leftrightarrow\; \gamma^2=1+\mathbf{u}_\perp^2+u_z^2$$

and

$$\gamma-u_z=\kappa;$$

combining these two equations, we obtain the simple result [16,18]

$$\theta(\gamma)=\arctan\sqrt{\frac{-1-\kappa_0^2+2\gamma\kappa_0}{\gamma^2+\kappa_0^2-2\gamma\kappa_0}}=\arctan\left[\frac{\sqrt{\left(\frac{2}{1+\beta_0}\right)\left(\frac{\gamma}{\gamma_0}-1\right)}}{\gamma-\gamma_0(1-\beta_0)}\right]. \tag{10}$$

For focusing waves, the light-cone variable is no longer invariant and the relation described by Eq. (10) is not strictly valid anymore.

III. THREE-DIMENSIONAL FOCUSING

In vacuum, the wave equation takes the familiar form

$$\left[\nabla^2-\frac{1}{c^2}\,\partial_t^2\right]A_\mu=[\partial_\nu\partial^\nu]A_\mu=0, \tag{11}$$

where we have introduced the 4-gradient operator $\partial_\mu\equiv\partial/\partial X^\mu\equiv[-(1/c)\partial_t,\boldsymbol{\nabla}]$ and the 4-potential $A_\mu\equiv(\varphi/c,\mathbf{A})$, which is chosen to satisfy the Lorentz gauge condition

$$\partial_\mu A^\mu=0. \tag{12}$$

The electromagnetic field tensor is defined by $F_{\mu\nu}=\partial_\mu A_\nu-\partial_\nu A_\mu$.

A. Exact three-dimensional solution

In vacuum, a general solution to the wave equation can be constructed as a Fourier superposition of wave packets of the form

$$A_\mu(x_\nu)=\frac{1}{(2\pi)^2}\int\!\!\int\!\!\int\!\!\int\tilde{A}_\mu(k_\nu)\exp(ik_\nu x^\nu)d^4k_\lambda, \tag{13}$$

where the notation d^4k_λ represents the differential 4-volume $\Pi_\lambda dk_\lambda=dk_0dk_1dk_2dk_3$ and the 4-wave-number $k_\mu\equiv(\omega/c,\mathbf{k})$ satisfies the vacuum dispersion relation

$$\frac{\omega^2}{c^2}-\mathbf{k}^2=k_\mu k^\mu=0, \tag{14}$$

which is also the mass shell condition for the photon field: $\hbar^2(k_\mu k^\mu)=0$. In Cartesian coordinates, this translates into

$$A_\mu(x,y,z,t)=\frac{1}{(2\pi)^2}\int\!\!\int\!\!\int\!\!\int\tilde{A}_\mu(\mathbf{k},\omega)\times\exp[i(\omega t-\mathbf{k}\cdot\mathbf{x})]d^3\mathbf{k}\,d\omega. \tag{15}$$

In the case where the laser pulse characteristics are defined at focus ($z=0$), we can obtain the electromagnetic field distribution in any given z plane by performing the integral (i.e., by applying the propagation operator)

$$A_\mu(x,y,z,t)=\frac{1}{(2\pi)^{3/2}}\int\int\int\tilde{A}_\mu(\mathbf{k}_\perp,\omega,z=0)\times\exp\left[i\left(\omega t-k_xx-k_yy-\sqrt{\frac{\omega^2}{c^2}-\mathbf{k}_\perp^2}z\right)\right]d^2\mathbf{k}_\perp d\omega. \tag{16}$$

This solution is easily interpreted: The temporal evolution of each wave packet is described by the frequency spectrum, while the transverse profile of the laser wave is expressed as

an integral over a continuous spectrum of transverse vacuum eigenmodes. The dispersion relation indicates how each transverse component of the wave packet propagates, thus yielding wave-front curvature and transverse spreading (diffraction) of the wave packet. It should also be noted that the axial wave number can become purely imaginary, in which case the corresponding waves become evanescent modes. In Eq. (16) we have introduced the frequency and transverse wave-number spectral distributions at focus, which are determined by Fourier transforming the local field distribution according to

$$\tilde{A}_\mu(\mathbf{k}_\perp,\omega,z=0)=\frac{1}{(2\pi)^{3/2}}\int\int\int A_\mu(x,y,z=0,t)\times\exp[-i(\omega t-k_x x-k_y y)]dx\,dy\,dt. \tag{17}$$

The next consideration is the gauge condition, which can be chosen to reduce to the Coulomb gauge $\nabla\cdot\mathbf{A}=0$ in a frame where the scalar potential is set to zero. Such a divergence-free vector potential can be generated by a vector field $\mathbf{G}$, defined such that $\mathbf{A}=\nabla\times\mathbf{G}$. As the curl and d'Alembertian operators commute, it is clear that if $\mathbf{G}$ satisfies the propagation equation, the vector potential will also satisfy it. For an electromagnetic wave propagating along the z axis and linearly polarized in the x direction, the generating vector field reduces to $\mathbf{G}(x_\mu)=\hat{y}G_y(x_\mu)$. For a Gaussian-elliptical focus, the generating field takes the form

$$G_y(x,y,z=0,t)=\frac{A_\perp}{k_0}\exp\left[-\left(\frac{x}{w_{0x}}\right)^2-\left(\frac{y}{w_{0y}}\right)^2\right]h(t), \tag{18}$$

where w_{0x} refers to the beam waist along the x axis and w_{0y} refers to the beam waist along the y axis, $A_\perp$ is the amplitude of the vector potential at focus, $k_0=\omega_0/c=2\pi/\lambda_0$ corresponds to the central laser wavelength, and $h(t)$ is the temporal variation of the laser wave, which can be arbitrary. The corresponding focal spectral density is

$$\tilde{G}_y(\mathbf{k}_\perp,\omega,z=0)=\frac{A_\perp}{2k_0}w_{0x}w_{0y}\tilde{h}(\omega)\times\exp\left[-\left(\frac{k_x x}{2}\right)^2-\left(\frac{k_y y}{2}\right)^2\right]. \tag{19}$$

The propagation integral then takes the form

$$G_y(x,y,z,t)=\frac{1}{(2\pi)^{3/2}}\int\int\int\tilde{G}_y(\mathbf{k}_\perp,z=0,\omega)\times\exp\left[i\left(\omega t-k_x x-k_y y-\sqrt{\frac{\omega^2}{c^2}-k_\perp^2}\,z\right)\right]d^2\mathbf{k}_\perp d\omega, \tag{20}$$

which is an exact solution to the three-dimensional wave equation in vacuum. The corresponding vector potential is obtained by taking the curl of the generating field $\mathbf{G}$.

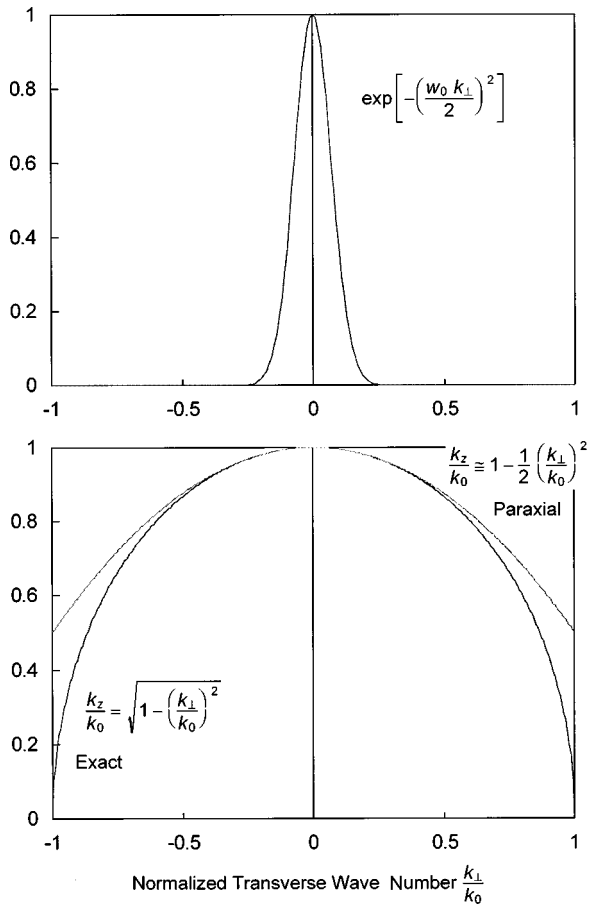

FIG. 2. Normalized transverse wave-number spectrum (top) and the exact and paraxial phase (bottom). The beam waist to wavelength ratio is $w_0/\lambda_0=10/\pi$.

B. Paraxial propagator

The three-dimensional behavior of the laser electromagnetic field is now described within the context of the paraxial propagator formalism. Here the photon mass shell condition is approximated by a quadratic Taylor expansion, namely, Eq. (20) is replaced by

$$G_y(x,y,z,t)=\frac{1}{(2\pi)^{3/2}}\int\int\int\tilde{G}_y(\mathbf{k}_\perp,z=0,\omega)\times\exp\left\{i\left[\omega t-k_x x-k_y y-\left(\frac{\omega}{c}-\frac{k_\perp^2}{2k_0}\right)z\right]\right\}d^2\mathbf{k}_\perp d\omega, \tag{21}$$

where the square root factor has been Taylor expanded to second order around $\omega=\omega_0$ and $\mathbf{k}_\perp=\mathbf{0}$. It is clear that the exact and Taylor expanded axial phases differ only for large values of the transverse wave number, where the spectral density is vanishingly small.

The physical content of the paraxial approximation is illustrated in Fig. 2. The Gaussian transverse wave-number spectrum is shown for $w_0k_0=20$, where $k_0=2\pi/\lambda_0$. Evanescent modes correspond to $k_\perp/k_0>1$. The axial wave number is also shown both for the exact dispersion relation

and in the paraxial approximation. It is clear that for physically realizable foci, where the beam waist is significantly larger than the wavelength, the region of transverse wave-number space where the paraxial phase differs significantly from the exact value corresponds to very small spectral amplitudes. For larger values of the f number, the transverse wave-number spectrum is narrower and the approximation is even better.

Inserting the Gaussian spectral density from Eq. (19) into Eq. (21), we see that the integration over ω is a simple Fourier transform of $\tilde{h}(\omega)$ and yields $h(t-z/c)=h(\phi/\omega_0)$. The integrals over the transverse momentum are also readily obtained, as they correspond to exponentials of quadratic complex polynomials [43]:

$$
\begin{aligned}
G_y(x,y,z,t)=&\frac{A_\perp}{k_0}\,h\left(\frac{\phi}{\omega_0}\right)\left[1+\left(\frac{z}{z_{0x}}\right)^2\right]^{-1/4}\\
&\times\left[1+\left(\frac{z}{z_{0y}}\right)^2\right]^{-1/4}\\
&\times\exp\left\{-\left[\frac{x}{w_x(z)}\right]^2-\left[\frac{y}{w_y(z)}\right]^2\right\}\\
&\times\exp\left[i\left\{\frac{1}{2}\arctan\left(\frac{z}{z_{0x}}\right)\right.\right.\\
&+\frac{1}{2}\arctan\left(\frac{z}{z_{0y}}\right)-\frac{z}{z_{0x}}\left(\frac{x}{w_x(z)}\right)^2\\
&\left.\left.-\frac{z}{z_{0y}}\left(\frac{y}{w_y(z)}\right)^2\right\}\right],
\end{aligned}
\tag{22}
$$

where $w_{x,y}(z)=w_{0x,y}\sqrt{1+(z/z_{0x,y})^2}$ are the waist sizes and $z_{0x,y}=\frac{1}{2}k_0w_{0x,y}^2$ represent the Rayleigh ranges for each f number, which are defined by the relation $w_{0x,y}=\lambda_0/\pi\,\arctan(1/2\,f_{x,y})$ [23–25].

Finally, taking the real part of the curl of the generating vector, we derive the vector potential

$$
\begin{aligned}
\frac{\mathbf{A}(x_\mu)}{\mathrm{Re}[G_y(x_\mu)]}=&\hat{x}\left\{\frac{k_0}{g(\phi)}\frac{dg}{d\phi}+\frac{z}{2(z^2+z_{0x}^2)}\right.\\
&\times\left[1-\left(\frac{2x}{w_x}\right)^2\right]+\frac{z}{2(z^2+z_{0y}^2)}\\
&\left.\times\left[1-\left(\frac{2y}{w_y}\right)^2\right]+\tan(\Lambda)\,\frac{\partial\Lambda}{\partial z}\right\}\\
&+\hat{z}\left[\frac{k_0xz}{(z^2+z_{0x}^2)}\tan(\Lambda)-\frac{2x}{w_x^2}\right],
\end{aligned}
\tag{23}
$$

where we have written the temporal laser pulse in terms of a slowly varying envelope $h(\phi)=g(\phi)e^{i\phi}$. In Eq. (23) the total phase is given by

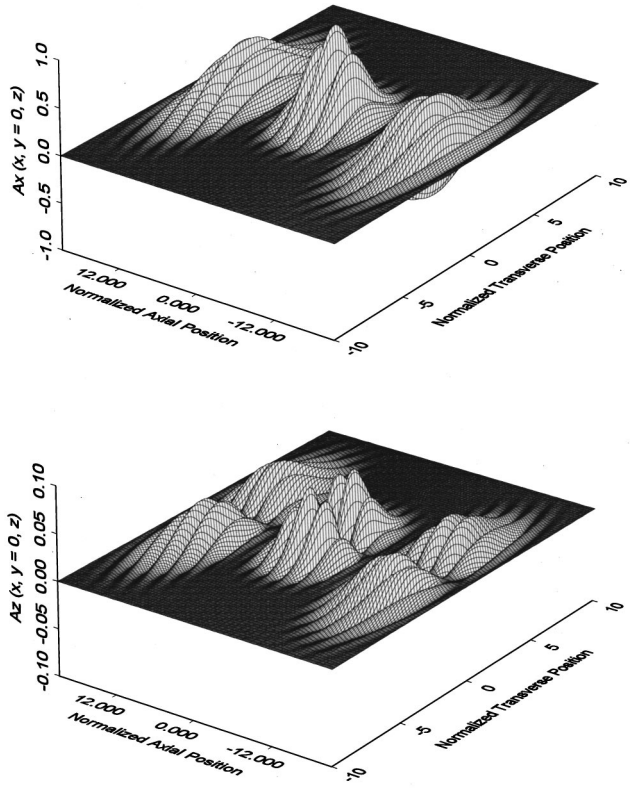

FIG. 3. Transverse and axial vector potential components, in the plane of polarization, at three different times. The pulses are six cycles long and $f=3$.

$$
\begin{aligned}
\Lambda=\phi+\frac{1}{2}\left[\arctan\left(\frac{z}{z_{0x}}\right)+\arctan\left(\frac{z}{z_{0y}}\right)\right.\\
\left.-\frac{k_0zx^2}{z^2+z_{0x}^2}-\frac{k_0zy^2}{z^2+z_{0y}^2}\right],
\end{aligned}
\tag{24}
$$

which includes the Guoy phase [23–25].

The vector potential of the focusing wave is shown in Fig. 3. The fields are then derived from this vector potential. We note that in the plane of polarization ($y=0$), only E_x, E_z, and B_y are nonzero; as a result, electrons seeded at $y=0$, with no momentum component in the y direction, will remain in this plane.

We have thus derived a general solution to the wave equation in vacuum, which reduces to the paraxial approximation in the limit of small transverse wave numbers. In addition, the derivation of an analytical expression of the axial field component in the case of linear polarization, within this approximation, will prove quite useful to study the relativistic dynamics of electrons in ultrahigh-intensity laser fields. In particular, this derivation can be extended to higher-order Gaussian modes, which are thought to yield the particle confinement [38] required for vacuum laser acceleration applications [1–18].

We also note that the extension of the above considerations to circular polarization can be achieved in a very straightforward manner: The generating field simply takes the form

$$\mathbf{G}(x,y,z=0,t)=\frac{A_\perp}{k_0}\exp\left[-\left(\frac{x}{w_{0x}}\right)^2-\left(\frac{y}{w_{0y}}\right)^2\right]\times g(t)[\hat{x}\,\sin(\omega_0 t)+\hat{y}\,\cos(\omega_0 t)]. \tag{25}$$

Here again $g(t)$ can be an arbitrary function of time.

Finally, Eq. (22) takes a more familiar form for a cylindrical focus

$$G_y(x,y,z,t)=\frac{A_\perp}{k_0}\,h\left(\frac{\phi}{\omega_0}\right)\frac{\exp\left\{-\left[\frac{r}{w(z)}\right]^2\right\}}{\sqrt{1+\left(\frac{z}{z_0}\right)^2}}\times\exp\left[i\left\{\arctan\left(\frac{z}{z_0}\right)-\left(\frac{z}{z_0}\right)\left(\frac{r}{w(z)}\right)^2\right\}\right], \tag{26}$$

where we recognize the Rayleigh range, Guoy phase, and wave-front curvature [23–25].

This formalism can also be studied in cylindrical coordinates, where the radial dependence of the focusing wave is described as a continuous spectrum of Bessel functions, and can be obtained by using Hankel's integral theorem. To define the boundary conditions for this problem, the beam profile is matched to a Gaussian-Hermite distribution at focus, where the wave front is planar. This derivation is presented in the Appendix and its equivalence to the Cartesian coordinate approach is established.

IV. NUMERICAL SIMULATIONS AND PONDEROMOTIVE SCATTERING

In this section we first present numerical calculations pertaining to the comparison between the paraxial ray approximation and the exact mathematical procedures introduced in Sec. III. We are primarily concerned with linearly polarized waves that have a Gaussian radial intensity distribution at focus. The numerical methods presented here can easily be extended to more complex focal distributions. In addition, we first consider monochromatic waves, so that the temporal Fourier transform is not necessary. Again, the generalization to broadband, ultrashort laser pulses is readily achieved by means of a Fourier integral over the laser frequency spectrum, as discussed in Sec. III B.

In our numerical simulations, Eq. (16) is evaluated numerically for the case of a monochromatic, linearly polarized pulse having a Gaussian radial intensity distribution at focus, with a relative accuracy in the 10^{-8} range [44]. The convergence of the code is verified by first considering the focus, where the code performs the exact integral, which is then compared to the input focal distribution. For typical parameters, such as those shown in Fig. 4, the convergence to the input Gaussian is excellent over 10–11 orders of magnitude.

The axial field component is evaluated in the following manner: For the paraxial ray approximation, we use the expression derived in Eq. (23) and take $w_{0x}=w_{0y}=w_0$, while

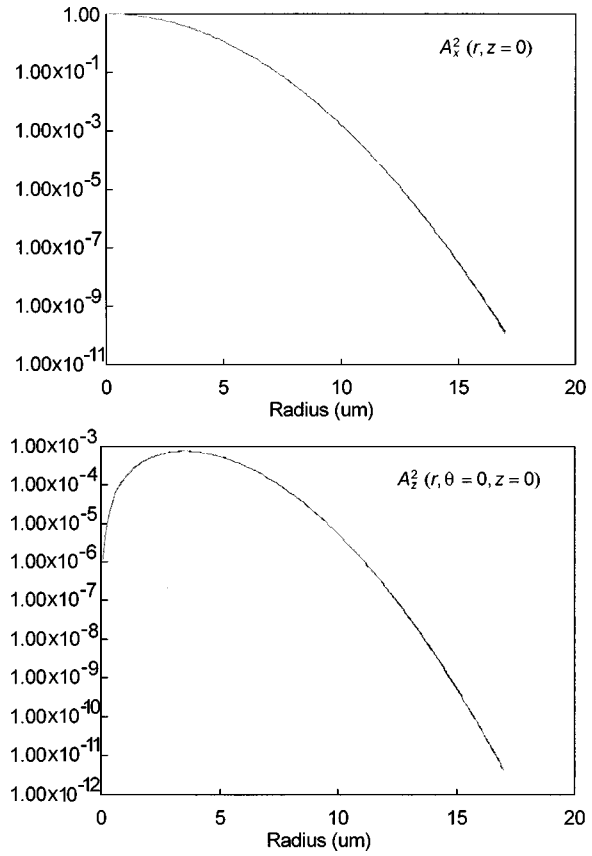

FIG. 4. Transverse (top) and axial (bottom) 4-potential components (amplitude squared) at focus, as functions of radius for $w_0=5\ \mu$m and $\lambda_0=1\ \mu$m, on a logarithmic scale.

the exact expression is given by Eq. (16). The agreement between both expressions at focus confirms the accuracy of the code. In addition, this level of agreement is maintained over a wide range of focal beam waists (from 1.5 μm to 1 mm). As expected, the axial field component vanishes on axis ($r=0$) and in the $x=0$ plane. It is also interesting to note that the axial component is much smaller than the transverse component because of the modest wave-front curvature. For reference, the intensity distributions are also shown in linear scale in Fig. 5 for the same parameters ($w_0=5\ \mu$m and $\lambda_0=1\ \mu$m).

In Fig. 6 the wave has propagated over ten Rayleigh ranges, and the diffraction is compared for the exact and paraxial solutions to the wave equation. Again, good agreement is obtained over more than six orders of magnitude, as expected because of the weak wave-front curvature. Some numerical noise is visible at large radii ($>150\ \mu$m).

Using the code, a wide region of parameter space (f number and distance from focus) was mapped rather extensively, showing the robust validity of the paraxial ray approximation. In fact, the only systematic deviations between the code and the paraxial approximation were obtained for tight foci (1.5-μm beam waist at 1-μm wavelength) and far away from the focal region. An example is shown in Fig. 7, where $z/z_0=100$ (100 Rayleigh ranges away from focus). For both the transverse and axial field components, the exact solution is seen to diffract faster than the Gaussian spherical waves corresponding to the paraxial wave equation. However, this effect is significant only at large radii. Therefore, the paraxial

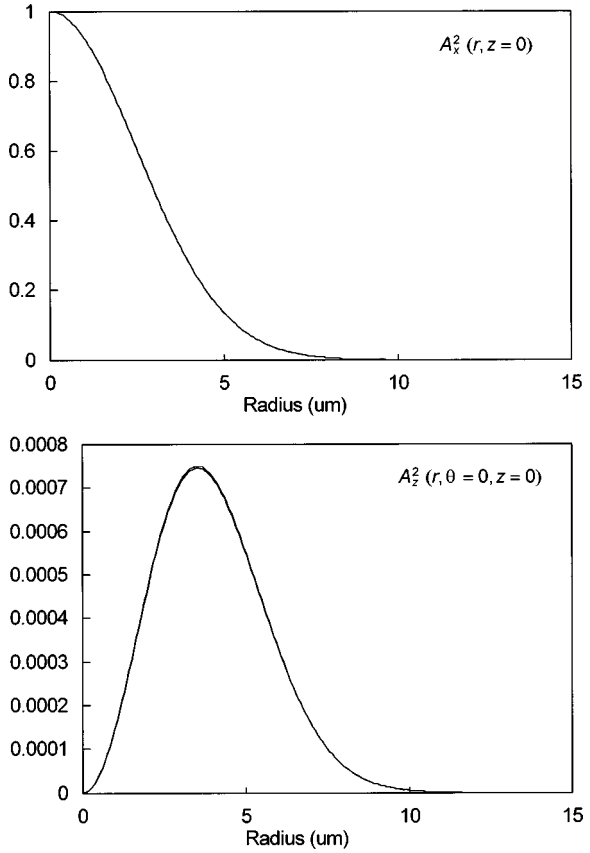

FIG. 5. Transverse (top) and axial (bottom) 4-potential components (amplitude squared) at focus, as functions of radius for $w_0 = 5\ \mu$m and $\lambda_0 = 1\ \mu$m, on a linear scale.

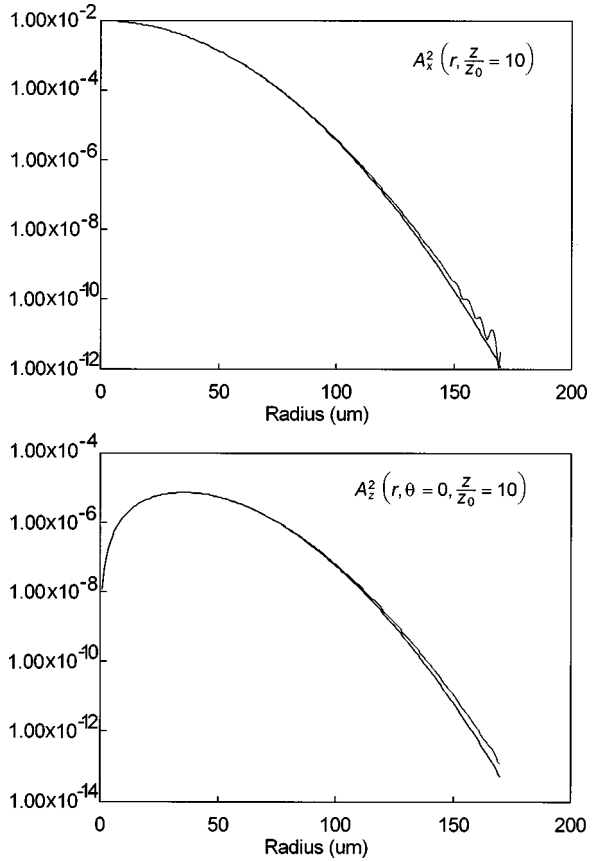

FIG. 6. Transverse (top) and axial (bottom) 4-potential components (amplitude squared) at $z/z_0 = 10$, as functions of radius for $w_0 = 5\ \mu$m and $\lambda_0 = 1\ \mu$m, on a logarithmic scale.

ray approximation is extremely well suited for studying nonlinear electron-laser interactions that are confined within a reasonably large radius from the propagation axis. In a real experimental situation, imperfect laser spatial filtering, as well as prepulses and other noisy phenomena, is expected to dominate over any deviations associated with the paraxial approximation.

Having obtained analytic expressions for the 4-potential, the Lorentz force equation may now be numerically integrated to yield the dynamics of a charge interacting with the three-dimensional laser fields. The algorithm developed for this purpose employs the second-order Runge-Kutta method and utilizes the axial electron phase as the variable of integration in order to handle both the nonlinear slippage and the large relativistic Doppler shift. The normalized equations of motion are

$$\frac{d\mathbf{u}}{d\phi} = -\frac{1}{\kappa}(\gamma\mathbf{e} + \mathbf{u}\times\mathbf{b}), \tag{27}$$

$$\frac{d\gamma}{d\phi} = -\frac{1}{\kappa}\mathbf{u}\cdot\mathbf{e}, \tag{28}$$

where we have introduced the normalized fields $\mathbf{e} = e\mathbf{E}/\omega_0 m_0 c$ and $\mathbf{b} = e\mathbf{B}/\omega_0 m_0$. The inverse of the light-cone variable is evaluated using the expression $1/\kappa = (\gamma + u_z)/(1+\mathbf{u}_\perp^2)$ to avoid divergences. In addition, the evolution equation for the light-cone variable

$$\frac{d\kappa}{d\phi} = -\frac{1}{\kappa}(\mathbf{u}\cdot\mathbf{e} - \gamma e_z - u_x b_y + u_y b_x), \tag{29}$$

is used to randomize the numerical noise and minimize the growth of numerical instabilities by introducing the averaged quantities

$$\langle\kappa\rangle = \frac{1}{2}\left[\int_0^\phi \frac{d\kappa}{d\psi}\,d\psi + \frac{1+\mathbf{u}_\perp^2}{\gamma+u_z}\right],$$

$$\langle\gamma\rangle = \frac{1}{2}\left[\int_0^\phi \frac{d\gamma}{d\psi}\,d\psi + \sqrt{1+\mathbf{u}^2}\right].$$

Note that for very large f numbers, Eq. (29) tends to zero and we recover the fact that the light-cone variable is an invariant for plane waves. The electron position is now given by $\mathbf{x}(\phi) = (c/\omega_0)\int_0^\phi (\mathbf{u}/\kappa)(\psi)\,d\psi$.

For a laser focus with extremely large f numbers, which should closely approximate a plane wave, excellent agreement is found between the corresponding numerical results and the theoretical analytic expressions obtained for plane-wave dynamics, as shown in Fig. 8 (top). For smaller values of f, scattering is obtained, as shown in Fig. 8 (bottom). In each case, the relative numerical error is in the 10^{-12}–10^{-16} range. It is interesting to note that for the parameters shown in Fig. 8 (bottom), the scattering energy is smaller than the maximum energy predicted by plane-wave theory. This is

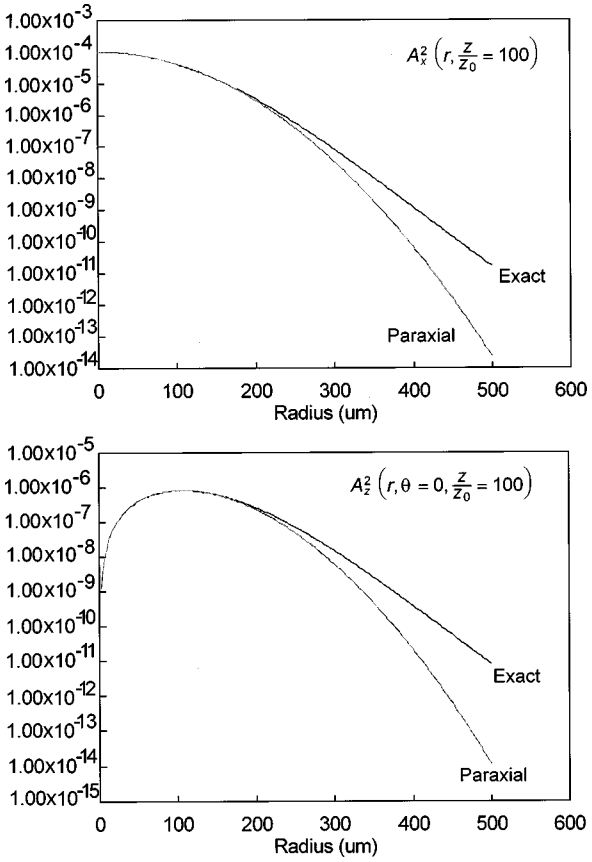

FIG. 7. Transverse (top) and axial (bottom) 4-potential components (amplitude squared) at $z/z_0=100$, as functions of radius for $w_0=1.5\ \mu$m and $\lambda_0=1\ \mu$m, on a logarithmic scale.

due to the fact that to obtain optimum scattering the electron phase must reach the temporal maximum of the drive pulse precisely at focus in order to experience the peak field of the laser. In general, the electron scatters from a spatiotemporal location other than this optimum point, at lower energies. The temporal pulse envelope is modeled by the function $g(\phi)=\sin^2[\pi(\phi/\omega_0\Delta t)]$ in order to integrate the equations of motion over a *finite* phase interval. The full width at half maximum (FWHM) of such a pulse is $\Delta t/2$.

To study this phenomenon systematically, we have examined the influence of the focus ellipticity and size. The results are shown in Fig. 9. Note that to obtain efficient scattering, the electron must be seeded far from focus, so that by the time it has slipped into the nonlinear temporal phase of the pulse, the focus is reached and the electron interacts with the spatiotemporal maximum of the laser wave. We observe that high-energy scattering occurs for intermediate values of the *f* numbers: For low values, the focus is too tight and the electron scatters away with minimal energy gain; for very large values, we recover the plane-wave interaction, with no energy gain. The fact that, for higher initial injection energies, efficient scattering (close to the plane-wave scaling) requires larger values of the *f* number is not surprising since the transverse electron excursion scales like $1/\kappa\cong 1/\kappa_0=\gamma_0(1+\beta_0)$. The largest scattering energies are achieved for $f_x>f_y$, which is directly related to the linear polarization of the drive laser. The high degree of symmetry of the surface with respect to f_x and f_y, however, indicates that the electron phasing, which is strongly influenced by the wave-front

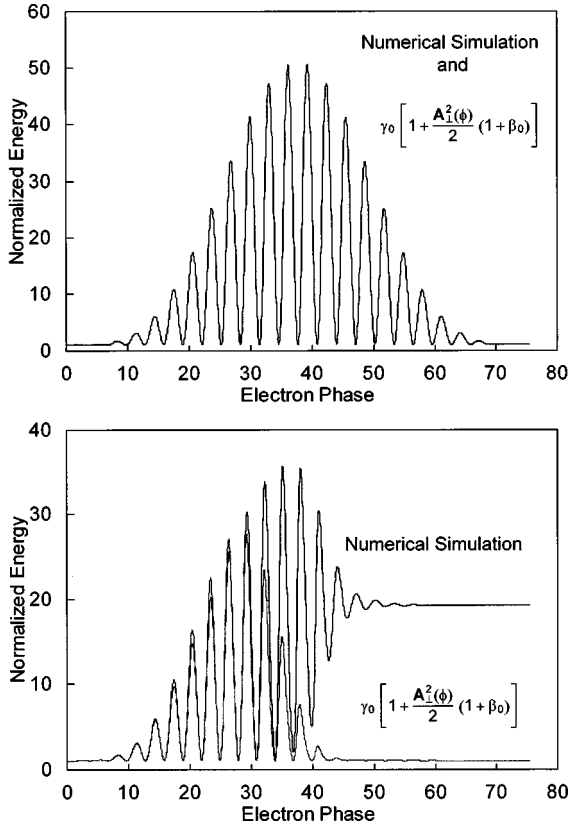

FIG. 8. Top, plane-wave interaction ($f_x=10^{20}$ and $f_y=10^{20}$); bottom, scattering ($f_x=5, f_y=5$). The other parameters are $A_\perp=10, \lambda_0=1\ \mu$m, a FWHM of 20 fs, no initial energy, and $x_i=y_i=0$; the initial axial position is at focus.

curvature, is of paramount importance. It also shows that cylindrical foci can be used for high-energy scattering.

To assess the feasibility of laser acceleration based on this scattering process, the total energy in the laser pulse is obtained by integrating the Poynting vector flux over the focal spot and the pulse duration to obtain

$$\frac{W}{m_0c^2}=\frac{3\pi}{32}A_\perp^2\frac{w_{0x}}{\lambda_0}\frac{w_{0y}}{\lambda_0}\frac{c\Delta t}{r_0}, \tag{30}$$

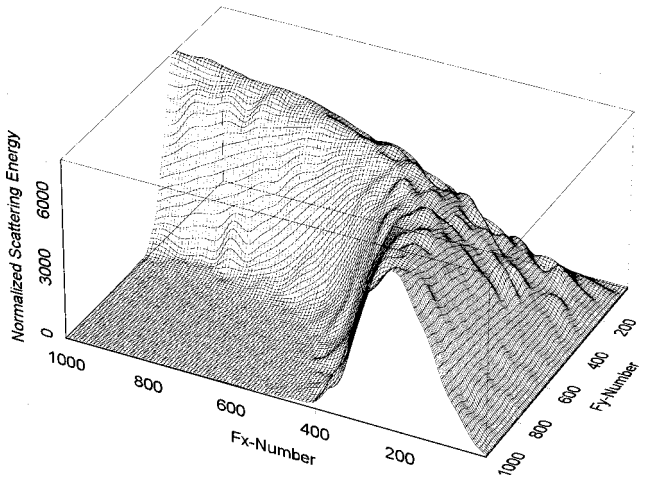

FIG. 9. Scan of f_x and f_y. The other parameters are $A_\perp=10, \lambda_0=1\ \mu$m, a FWHM of 20 fs, an initial energy of 10 MeV, $x_i=y_i=0$, and an initial axial position of -3 mm.

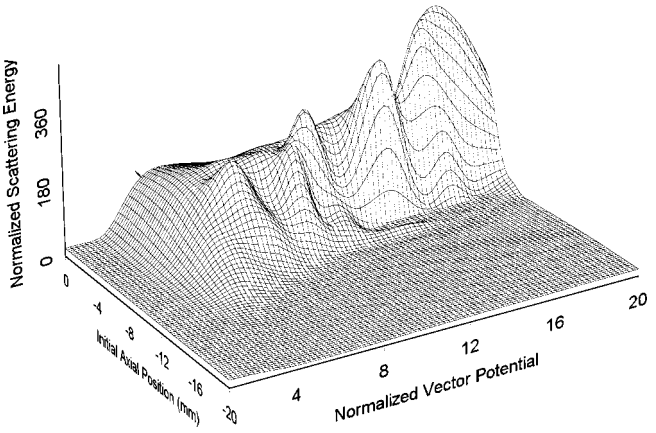

FIG. 10. Scan of $A_\perp$ and initial z for a constant pulse energy of 20 J. $\lambda_0=1\ \mu$m, the FWHM is 20 fs, the initial energy is 10 MeV, and $x_i=y_i=0$.

where $r_0=e^2/4\pi\varepsilon_0 m_0 c^2=2.817\ 85\times10^{-15}$ m is the classical electron radius. We then study a cylindrical focus ($w_{0x}=w_{0y}=w_0$), and maintain the pulse FWHM at 20 fs and the product $A_\perp w_0$ at 250 μm (constant energy of 20 J), while varying $A_\perp$ between 1 and 20 and varying the injection position between -20 mm and focus. The results are shown in Fig. 10, and clearly indicate the existence of an optimum combination of f number and laser intensity for high-energy scattering, approximately obtained for a normalized vector potential of 17.5 and $f=23$. Here, there is a sharply defined acceptance range in the initial position and the scattering energy reaches 0.25 GeV. The acceleration process occurs over a distance of 3 mm, yielding a gradient of 85 GeV/m. The laser parameters presented here should correspond to the next generation of chirped pulse laser amplifiers [46,47].

V. CONCLUSIONS

Exact solutions to the wave equation in vacuum have been studied for a three-dimensional laser focus for both rectangular and cylindrical geometries. Furthermore, it has been shown that the paraxial ray approximation corresponds to the quadratic Taylor expansion of the phase in the transverse wave number. Within this framework, in addition to the standard paraxial approximation of the transverse field component, an expression for the axial field component required to satisfy the gauge condition for linear polarization has been obtained, as well as the paraxial gauge condition itself. To our knowledge, these results represent an extension of the paraxial ray model of Gaussian spherical waves. While these results were obtained for linearly polarized waves and Gaussian foci, the formalism presented here can be generalized to describe circularly polarized and Gaussian-Hermite modes. Furthermore, the paraxial approximation has been extensively compared to the aforementioned exact solution and found to be in excellent agreement in most cases, thus justifying the general use of Gaussian spherical waves to model focusing waves in vacuum. The paraxial wave and gauge equations, and their solution for linear polarization, including the axial field component, are thus important results needed to model the nonlinear dynamics of relativistic electrons in the focus of an ultrahigh-intensity laser.

Finally, the relativistic dynamics of an electron submitted to the three-dimensional field of a focused, ultrahigh-intensity laser pulse have been studied numerically. The diffracting field in vacuum is modeled by the paraxial propagator and satisfies the gauge condition. Plane-wave dynamics are verified for large f numbers, including canonical momentum invariance. Scattering is predicted for smaller values of f at relativistic laser intensities and GeV electrons could be produced in vacuum using femtosecond laser pulses with energies in the 10–100 J range.

ACKNOWLEDGMENTS

This work was partially supported under the auspices of the U.S. Department of Energy by the Lawrence Livermore National Laboratory under Contract No. W-7405-ENG-48 through the Institute for Laser Science and Applications. Additional support was provided by DoD/AFOSR (MURI) Grant No. F49620-95-1-0253, AFOSR (ATRI) Grant No. F30602-94-2-001, and ARO Grant No. DAAHO4-95-1-0336. F. V. H. wishes to thank D. T. Santa Maria for very stimulating discussions.

APPENDIX: CYLINDRICAL FOCUSING GEOMETRY

1. Cylindrical wave equation

A number of experimental situations involve laser foci with cylindrical symmetry. It is therefore of interest to study the vacuum eigenmodes of this particular geometry. For cylindrical symmetry, the wave equation now reads [39]

$$\left[\nabla^2-\frac{1}{c^2}\,\partial_t^2\right]A_r-\frac{1}{r^2}\,(A_r+2\,\partial_\theta A_\theta)=0, \tag{A1}$$

$$\left[\nabla^2-\frac{1}{c^2}\,\partial_t^2\right]A_\theta-\frac{1}{r^2}\,(A_\theta-2\,\partial_\theta A_r)=0, \tag{A2}$$

$$\left[\nabla^2-\frac{1}{c^2}\,\partial_t^2\right]A_z=0, \tag{A3}$$

$$\left[\nabla^2-\frac{1}{c^2}\,\partial_t^2\right]\phi=0. \tag{A4}$$

The standard procedure to find a general solution to the cylindrical wave equation is to employ the method of separation of variables. The axial and temporal dependence of the 4-vector potential is represented by a double Fourier transform, while symmetry imposes harmonic dependence on the azimuthal angle. We thus have

$$\begin{aligned}A_\mu(x_\mu)&=A_\mu(r,\theta,z,t)\\&=\frac{1}{2\pi}\sum_m\int_{-\infty}^{+\infty}\int_{-\infty}^{+\infty}\tilde{A}_m(k_\parallel,\omega)R_{\mu m}(r)\\&\quad\times\exp[i(\omega t-k_\parallel z+m\theta)]dk_\parallel d\omega.\end{aligned} \tag{A5}$$

Inserting Eq. (A5) into the cylindrical wave equation and using the orthogonality of complex exponentials, we obtain two sets of differential equations corresponding to two families of modes: TE and TM.

The TM modes are generated by the axial and temporal components of the 4-potential. The corresponding wave equation admits solutions of the form [39,44]

$$R_{zm}(r)=R_{\|m}J_m(k_\perp r), \tag{A6}$$

$$R_{tm}(r)=R_{\|m}\frac{kc^2}{\omega}J_m(k_\perp r), \tag{A7}$$

where the transverse eigenwave number is constrained by the vacuum dispersion relation $\omega^2/c^2=k_\|^2+k_\perp^2$. In Eqs. (A6) and (A7) the constants have been adjusted for the axial and temporal components in order to satisfy the Lorentz gauge condition.

On the other hand, the TE modes are generated by the radial and azimuthal components of the 4-potential. The corresponding wave equation splits into two coupled differential equations, which admit solutions of the form [39,44]

$$R_{rm}(r)=R_{\perp m}\frac{J_m(k_\perp r)}{k_\perp r}, \tag{A8}$$

$$R_{\theta m}(r)=R_{\perp m}\frac{i}{m}J'_m(k_\perp r), \tag{A9}$$

where the transverse eigenvalue is again constrained by the dispersion relation. Note that here the gauge condition is automatically satisfied because the differential equations resulting from the wave equation are coupled.

In the case of a finite radial boundary at $r=a$ (cylindrical waveguide), the transverse eigenmode spectrum is discrete, and we have $k_\perp\equiv\chi'_{mn}/a$ for TE modes and $k_\perp\equiv\chi_{mn}/a$ for TM modes. Here χ'_{mn} and χ_{mn} are the nth zeros of J'_m and J_m, respectively [39,41]. However, in our case of interest, the radial boundary extends out to infinity and the radial eigenmode spectrum is continuous. In addition, the distinction between TE and TM modes breaks down since focusing waves correspond to hybrid modes.

It is interesting to note that since Bessel functions are the eigenmodes of the cylindrical wave equation in vacuum, these modes can theoretically propagate as plane waves [25], without diffracting. However, the dispersion relation shows that these modes are slow waves, with a nonzero cutoff frequency, thus indicating that such mode profiles cannot be maintained in vacuum, without a waveguide boundary condition. In addition, in a waveguide, the energy flow is limited by the finite radial extent of the structure, whereas in vacuum, the radial integral of a single unbounded Bessel function diverges [43–45].

We also note that, starting from these solutions, one can construct hybrid modes where the transverse components of the 4-potential correspond to TE-like modes and the axial component is described by a TM-like profile. However, here the gauge condition is satisfied differently from guided waves. For propagation in vacuum, such hybrid modes are required: e.g., in the case of a linearly polarized wave focusing in vacuum, a superposition of pure TE_{11} modes will not yield an adequate description since they are not truly linearly polarized, as shown in Fig. 11; therefore, an axial field component is required.

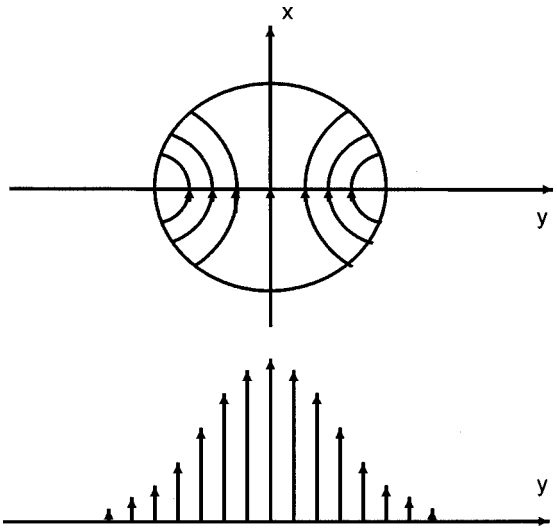

FIG. 11. Comparison between a TE_{11} mode and a linearly polarized Gaussian.

2. Vacuum eigenmode expansion and Fourier-Bessel transform

Now a general solution to the cylindrical wave equation can be expressed as a vacuum eigenmode expansion, but the continuous radial eigenvalue spectrum remains to be defined, namely, we have

$$A_\mu(r,\theta,z,t)=\frac{1}{2\pi}\sum_m\int\int\int\tilde{A}_m(k_\perp,k_\|,\omega)R_{\mu m}(k_\perp r)\times\exp[i(\omega t-k_\| z+m\theta)]dk_\perp dk_\| d\omega, \tag{A10}$$

where

$$R_{\mu m}(k_\perp r)=R_{\perp m}\left[\hat{r}\frac{J_m(k_\perp r)}{k_\perp r}+\hat{\theta}\frac{i}{m}J'_m(k_\perp r)\right] \tag{A11}$$

for the TE-like components and

$$R_{\mu m}(k_\perp r)=R_{\|m}J_m(k_\perp r)\left[\hat{z}+\hat{t}\frac{k_\| c^2}{\omega}\right] \tag{A12}$$

for the TM-like modes. The constraint between the radial eigenvalue and the frequency and wave number is given by the dispersion relation. This solution can easily be interpreted: The temporal evolution of the wave packet is described by its frequency spectrum, while the radial profile of the laser wave is described by an integral over a continuous spectrum of transverse vacuum eigenmodes (Bessel functions). The dispersion relation indicates how each radial and temporal component of the wave packet propagates, thus yielding wave-front curvature and diffraction of the wave packet. The polarization state is described by m. If the temporal and radial spectral distribution are known at a given position along the propagation axis, as well as the polariza-

tion state, the pulse characteristics can be obtained at any other axial position by following the corresponding procedure outlined in Sec. III A.

At this point, we need a mathematical procedure to determine the radial spectrum of the wave packet. The most relevant cases for practical applications correspond to linearly and circularly polarized wave packets, where the azimuthal number $|m|=1$. For example, in the case of a circularly polarized hyperbolic secant laser pulse with a Gaussian profile at focus, we have

$$A_r(r,\theta,z=0,t)=A\ \exp\left[-\left(\frac{r}{w_0}\right)^2\right]\frac{\cos(\omega_0 t-\theta)}{\cosh\left(\frac{t}{\Delta t}\right)}, \tag{A13}$$

$$A_\theta(r,\theta,z=0,t)=A\ \exp\left[-\left(\frac{r}{w_0}\right)^2\right]\frac{\sin(\omega_0 t-\theta)}{\cosh\left(\frac{t}{\Delta t}\right)}, \tag{A14}$$

where Δt is the pulse duration, ω_0 is the laser frequency, and w_0 is the focal beam waist. To express the Gaussian profile in terms of Bessel functions, one begins with Hankel's integral theorem, which reduces to Weber's integral in this case [40]. We have, for a Gaussian,

$$\int_0^\infty x e^{-a^2x^2}J_0(bx)dx=\frac{\exp(-b^2/4a^2)}{2a^2}. \tag{A15}$$

Because of the polarization constraint, we now express J_0 in terms of J_1, using the recurrence relation [40,43–45]

$$J_0(bx)=J_1'(bx)+\frac{J_1(bx)}{bx} \tag{A16}$$

to obtain

$$\frac{\exp(-b^2/4a^2)}{2a^2}=\int_0^\infty x e^{-a^2x^2}\left[J_1'(bx)+\frac{J_1(bx)}{bx}\right]dx, \tag{A17}$$

which is integrated by parts, yielding

$$\exp\left[-\left(\frac{b}{2a}\right)^2\right]=2a^2\left\{\left[x e^{-a^2x^2}\frac{1}{b}J_1(bx)\right]_0^\infty + \int_0^\infty 2a^2x^2e^{-a^2x^2}\frac{J_1(bx)}{b}dx\right\}. \tag{A18}$$

The first term in square brackets vanishes and we are left with the sought-after Bessel transform of a Gaussian

$$\exp\left[-\left(\frac{r}{w_0}\right)^2\right] = \frac{w_0^4}{4}\int_0^\infty k_\perp^3\exp\left[-\left(\frac{w_0k_\perp}{2}\right)^2\right]\frac{J_1(k_\perp r)}{k_\perp r}dk_\perp, \tag{A19}$$

where we have expressed the various parameters in terms of physical quantities. Performing the temporal Fourier transform of the circularly polarized hyperbolic secant pulse

$$\frac{\cos(\omega_0 t-\theta)}{\cosh\left(\frac{t}{\Delta t}\right)}=\frac{1}{\sqrt{2\pi}}\int_{-\infty}^{+\infty}\sqrt{\frac{\pi}{8}} \times\Delta t\ \frac{\exp[i(\omega t\pm\theta)]}{\cosh\left[\frac{\pi}{2}(\omega\pm\omega_0)\Delta t\right]}d\omega, \tag{A20}$$

the radial component of the 4-potential can now be evaluated at any point along the propagation axis by performing the integral

$$A_r=\frac{\Delta t w_0^4}{16}\int_{-\infty}^{+\infty}d\omega\int_0^\infty dk_\perp\ \frac{k_\perp^3\exp\left[-\left(\frac{w_0k_\perp}{2}\right)^2\right]}{\cosh\left[\frac{\pi}{2}(\omega\pm\omega_0)\Delta t\right]} \times\frac{J_1(k_\perp r)}{k_\perp r}\exp\left[i\left(\omega t-\sqrt{\frac{\omega^2}{c^2}-k_\perp^2}z\pm\theta\right)\right], \tag{A21}$$

where one must sum over the plus and minus signs. The azimuthal component of the 4-vector potential is obtained upon replacement of $J_1(k_\perp r)/k_\perp r$ by $iJ_1'(k_\perp r)$ in the integral. This procedure can be extended to Gaussian-Hermite profiles by noting that each term of the series has a Bessel transform given by Weber's integral [40]. Specifically, we have

$$r^n\exp\left[-\left(\frac{r}{w_0}\right)^2\right]=\left(\frac{w_0^2}{2}\right)^{n+1}\int_0^\infty k_\perp^{n+1} \times\exp\left[-\left(\frac{w_0k_\perp}{2}\right)^2\right]J_n(k_\perp r)dk_\perp. \tag{A22}$$

We then reduce the Bessel function order to 1, which is achieved by means of the recurrence relation [40,43–45] $J_{n-1}(k_\perp r)=n[J_n(k_\perp r)/k_\perp r]+J_n'(k_\perp r)$ and by integrating by parts. We have thus introduced a general mathematical procedure allowing for the exact description of the electromagnetic field distribution of a cylindrically symmetrical three-dimensional focus in vacuum, both in the near-field and in the far-field regions. The results derived here can also be obtained from the exact solution in rectangular coordinates (see Sec. III) by performing a coordinate transformation.

[1] M. J. Feldman and R. Y. Chiao, Phys. Rev. A **4**, 352 (1971).
[2] Ya. B. Zel'dovich, Sov. Phys. Usp. **18**, 79 (1975).
[3] V. N. Baier, V. M. Katkov, A. I. Mil'shtein, and V. M. Strakhovenko, Sov. Phys. JETP **42**, 400 (1975).
[4] J. Kruger and M. Bovyn, J. Phys. A **9**, 1841 (1976).
[5] J. A. Edighoffer and R. H. Pantell, J. Appl. Phys. **50**, 6120 (1979).
[6] W. M. Manheimer, Phys. Fluids **28**, 1569 (1985).
[7] S. Kawata, T. Maruyama, H. Watanabe, and I. Takahashi, Phys. Rev. Lett. **66**, 2072 (1991).
[8] M. S. Hussein and M. P. Pato, Phys. Rev. Lett. **68**, 1136 (1992).
[9] M. S. Hussein, M. P. Pato, and A. K. Kerman, Phys. Rev. A **46**, 3562 (1992).
[10] L. C. Steinhauer and W. D. Kimura, J. Appl. Phys. **72**, 3237 (1992).
[11] E. J. Bochove, G. T. Moore, and M. O. Scully, Phys. Rev. A **46**, 6640 (1992).
[12] T. Hauser, W. Scheid, and H. Hora, Phys. Lett. A **186**, 189 (1994).
[13] J. E. Moore and N. J. Fish, Phys. Plasmas **1**, 1105 (1994).
[14] N. B. Baranova, B. Ya. Zel'dovich, and M. O. Scully, JETP **78**, 249 (1994).
[15] E. Esarey, P. Sprangle, and J. Krall, Phys. Rev. E **52**, 5443 (1995).
[16] F. V. Hartemann *et al.*, Phys. Rev. E **51**, 4833 (1995).
[17] M. V. Fedorov, S. P. Goreslavsky, and V. S. Letokhov, Phys. Rev. E **55**, 1015 (1997).
[18] Y. I. Salamin and F. H. M. Faisal, Phys. Rev. A **55**, 3678 (1997).
[19] F. V. Hartemann, A. L. Troha, N. C. Luhmann, Jr., and Z. Toffano, Phys. Rev. E **54**, 2956 (1996).
[20] F. V. Hartemann and A. K. Kerman, Phys. Rev. Lett. **76**, 624 (1996).
[21] P. L. Kapitza and P. A. M. Dirac, Proc. Cambridge Philos. Soc. **29**, 297 (1933).
[22] P. H. Bucksbaum, L. D. Van Woerkom, R. R. Freemann, and D. W. Schumacher, Phys. Rev. A **41**, 4119 (1990).
[23] A. Yariv, *Quantum Electronics* (Wiley, New York, 1967), Chaps. 6 and 7.
[24] A. E. Siegman, *Lasers* (University Science Books, Mill Valley, CA, 1986), Chaps. 16–21.
[25] P. W. Milonni and J. H. Eberly, *Lasers* (Wiley Interscience, New York, 1988), Chap. 14.
[26] C. Bula *et al.*, Phys. Rev. Lett. **76**, 3116 (1996).
[27] G. Malka, E. Levebvre, and J. L. Miquel, Phys. Rev. Lett. **78**, 3314 (1997).
[28] T. Tajima and J. M. Dawson, Phys. Rev. Lett. **43**, 267 (1979).
[29] C. Joshi, T. Tajima, J. M. Dawson, H. A. Baldis, and N. A. Ebrahim, Phys. Rev. Lett. **47**, 1285 (1981).
[30] D. W. Forslund, J. M. Kindel, W. B. Mori, C. Joshi, and J. M. Dawson, Phys. Rev. Lett. **54**, 558 (1985).
[31] W. B. Mori, C. Joshi, J. M. Dawson, D. W. Forslund, and J. M. Kindel, Phys. Rev. Lett. **60**, 1298 (1988).
[32] C. E. Clayton, K. A. Marsh, A. Dyson, M. Everett, W. P. Leemans, R. Williams, and C. Joshi, Phys. Rev. Lett. **70**, 37 (1993).
[33] P. Sprangle, E. Esarey, and J. Krall, Phys. Plasmas **3**, 2183 (1996).
[34] J. Ojeda-Castaneda, J. C. Escalera, and M. J. Yzuel, Opt. Commun. **114**, 189 (1995).
[35] L. S. Brown and T. W. B. Kibble, Phys. Rev. **133**, A705 (1963).
[36] T. W. B. Kibble, Phys. Rev. **150**, 1060 (1966).
[37] E. S. Sarachik and G. T. Schappert, Phys. Rev. D **1**, 2738 (1970).
[38] C. I. Moore, J. Mod. Opt. **39**, 2171 (1992).
[39] F. V. Hartemann, Phys. Rev. A **42**, 2906 (1990).
[40] N. N. Lebedev, *Special Functions and their Applications* (Dover, New York, 1972), Chap. 5.
[41] J. D. Jackson, *Classical Electrodynamics* (Wiley, New York, 1975), Chaps. 8, 11, and 12.
[42] W. Pauli, *Theory of Relativity* (Dover, New York, 1958), Chaps. 27–34.
[43] I. S. Gradshteyn and I. M. Ryzhik, *Table of Integrals, Series and Products* (Academic, Orlando, 1980).
[44] E. Jahnke and F. Emde, *Tables of Functions* (Dover, New York, 1945), Chap. 8.
[45] *Handbook of Mathematical Functions*, edited by M. Abramowitz and I. A. Stegun (Dover, New York, 1965), Chap. 9.
[46] M. D. Perry and G. Mourou, Science **264**, 917 (1994).
[47] G. A. Mourou, C. P. J. Barty, and M. D. Perry, Phys. Today **51** (1), 22 (1998).